Nanoparticles Change the Ordering Pattern of *n*-Carboxylic Acids into Nanorods on HOPG

Ruomiao Wang,[†] Li Li,[†] Indika Arachchige,[‡] Shreyashi Ganguly,[‡] Stephanie L. Brock,[‡] and Guangzhao Mao[†,*]

[†]Department of Chemical Engineering and Materials Science, Wayne State University, 5050 Anthony Wayne Drive, Detroit, Michigan 48202, United States, and [‡]Department of Chemistry, Wayne State University, 5101 Cass Avenue, Detroit, Michigan 48202, United States

Physisorbed monolayers of amphiphiles are relevant to biological processes, lubrication, colloidal stabilization, detergency, patterning, and thin film devices.[1,2] Nanoparticle and/or nanowire arrays are employed in surface plasmon devices, surface-enhanced Raman scattering, single-electron devices, ion-sensitive field-effect transistors, and photocurrent generation modules.[3−5] A key challenge for maximizing functionality of devices lies in establishing methods for connecting these disparate nanocomponents: nanoparticles, nanowires, and monolayers, in predefined spatial arrangements with distinct interfaces.[6−12] Self-assembly, such as the self-aligning tendency of nanorods (due to capillary forces[13] and entropy-driven minimization of the excluded volume[14]), can be used to connect and align nano-objects. However, self-assembly strategies for nanocomponent integration, that is, interfacing individual nanoparticles and nanorods are few. Furthermore, most studies are focused on inorganic nanocrystal self-assemblies, but molecular self-assembly based on organic nanocrystals[15,16] or hybrid inorganic/organic nanostructures is also expected to yield unique (and perhaps improved) properties. For example, junctions between self-assembled monolayers and metal nanoparticles allow the study of single-electron transfer processes;[17] room-temperature light-emitting diodes have been created by the incorporation of a dye molecule within a perovskite framework;[18] and attachment of oligonucleotides to Au nanoparticles triggers the self-assembly of DNA/nanoparticle arrays for biosensing and DNA sequencing.[19] Similarly, a single-wall carbon nanotube (CNT) placed between two Au electrodes and coated with en-zymes shows higher detection sensitivity of enzyme activity.[20] Hybrid Au nanoparticle CNT catalysts show an enhanced electrochemical catalytic activity for the oxygen reduction reaction.[21] Finally, the incorporation of conductive Au nanoparticles with charge-transporting oligoaniline cross-linkers is shown to enhance the photocurrent generation of CdS nanoparticle arrays.[22]

This paper reports a method to self-assemble organic nanorods of *n*-carboxylic acids directly on thiolate-protected inorganic nanoparticles. Alkanes and alkane derivatives, such as *n*-carboxylic acids, physisorb on highly oriented pyrolytic graphite (HOPG) with their carbon chain skeletal plane parallel to the HOPG basal plane.[23−27] We find that nanoparticles are capable of

ABSTRACT This paper describes the formation of organic nanorods induced by monolayer-protected inorganic nanoparticles. Alkanes and alkane derivatives, such as *n*-carboxylic acids, self-assemble on highly oriented pyrolytic graphite (HOPG) into a persistent molecular packing structure that is dictated by the epitaxial interaction between the carbon chain plane and the HOPG basal plane. Carboxylic acids form 2-D crystalline layers consisting of nanostripe domains whose periodicity is one or two times the molecular chain length. However, when the molecular ordering occurs in the vicinity of a nanoparticle, this persistent HOPG-dominated nanostripe pattern is disrupted, and nanorods attached to the nanoparticles become the dominant structure. In order to understand the underlying mechanism of the nanoparticle-mediated nanorod formation, the effects of film-forming conditions, carboxylic acid chain length, nanoparticle size, and chemical composition of the nanoparticle are examined. It is determined that carboxylic acid nanorods can be induced by nanoparticles of different core materials including CdSe, CdS, and Au, as long as the protecting monolayer allows sufficient dispersion and colloidal stability of the nanoparticles in solution. A carboxylic chain length range amenable to the nanorod formation is identified, as is the relationship between the nanoparticle size and the number of nanorods per nanoparticle. This study contributes to the understanding of seed-mediated crystallization and molecular ordering. Moreover, it defines the parameters governing solution-based formation of hybrid nanostructures and nanopatterns incorporating dual functionality as defined by the inorganic nanoparticle and organic nanorod, respectively.

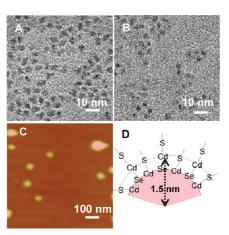**KEYWORDS:** self-assembly · hybrid nanostructure · AFM · nanorod · nanoparticle

Figure 1. TEM images of (A) TOPO-CdSe nanoparticles and (B) MUA-CdSe nanoparticles. (C) AFM height image of MUA-CdSe nanoparticles deposited on Mn²⁺-treated mica substrate (z range = 10 nm). (D) Schematic representation of a thiolate-capped CdSe nanoparticle with Cd in excess.

disrupting this persistent physisorbed pattern of n-carboxylic acids on HOPG. In our previous work, nanorods of eicosanoic acid (arachidic acid, $C_{20}A$) have been shown to nucleate on mercaptoundecanoic acid-capped CdSe nanoparticles (MUA-CdSe) on HOPG.[28] In the absence of MUA-CdSe, $C_{20}A$ forms an epitaxial pattern in the form of parallel nanostripes on HOPG with a periodicity of 5.6 nm—twice the $C_{20}A$ chain length. MUA-CdSe nanoparticles do not adsorb readily on HOPG; however, the nanoparticle/nanorod hybrid architecture forms spontaneously on HOPG from a mixed MUA-CdSe/$C_{20}A$ alcoholic solution during spin coating. The $C_{20}A$ nanorods possess uniform height (=1.0 nm) and width (=5.4 nm) despite the stochastic crystallization kinetics.[29,30] In the present work, we conduct experiments to probe the formation mechanism of the nanoparticle/nanorod structure by varying film-forming conditions, carboxylic acid chain length, nanoparticle size, and nanoparticle chemical composition, including the inorganic core and thiolate-protecting layer. The study contributes to the understanding of seed-mediated nucleation and crystallization, molecular ordering under nanoconfinement, and engineering of hybrid thin film materials.

RESULTS

Synthesis. Inorganic nanoparticle−organic nanorod hybrids are prepared from a combination of inorganic nanoparticles, CdSe, CdS, or Au, whose surfaces are modified by thiolates including MUA, mercaptopropionic acid (MPA), or dodecanethiol (DDT) and organic crystalline compounds n-carboxylic acids. For comparison, the film formation characteristics of nanoparticles and n-carboxylic acids are also studied independently.

Nanoparticle Size and Structural Analysis. TEM is used to determine the inorganic core size of the nanoparticles. TEM images of trioctylphosphine oxide (TOPO)-capped CdSe nanoparticles are displayed in Figure 1A,B. The av-

TABLE 1. AFM Sectional Height Analysis Results of the Nanoparticles Physisorbed on Mn²⁺-Treated Mica

nanoparticle (synthesis ratio)	vertical dimension (nm)	lateral dimension (nm)
MUA-CdSe (3:1)	4.7 ± 1.9	16.9 ± 4.6
MUA-CdSe (5:1)	5.8 ± 2.1	40.2 ± 10.0
MPA-CdSe (5:1)	7.3 ± 2.3	30.8 ± 6.8
MUA-CdS (5:1)	3.1 ± 0.9	24.7 ± 8.6
DDT-CdSe (10:1)	3.6 ± 0.5	19.6 ± 5.0

erage diameter of the CdSe nanoparticle core is determined to be 3.0 ± 0.6 nm. The nanoparticle size is also measured using AFM images of immobilized nanoparticles (Figure 1C) and AFM sectional height analysis (Table 1). In order to immobilize negatively charged nanoparticles on mica, we use a method previously developed for DNA immobilization:[31] 20 μL of 10^{-6} M $MnCl_2$ solution is placed on 1 cm² freshly cleaved mica to render the substrate positively charged. The nanoparticle height values are used because the lateral values are convoluted by the AFM probe. The AFM height values differ from the TEM diameters by the capping layer thickness. A closely packed MPA monolayer presumably adds ~1 nm, and an MUA monolayer adds ~3 nm to the overall particle diameter. The larger than expected size of MPA-CdSe is likely due to its tendency to aggregate.

The nanoparticle chemical compositions by EDAX are listed in Table 2. In the case of CdS nanoparticles, S content from the thiolate ligands is deduced from the difference of percentage of S in thiolate-capped and in TOPO-capped CdS nanoparticles. The results indicate that there is an excess of Cd in all of the nanoparticles. Figure 1D is a schematic representation of CdSe with excess Cd near the surface (a similar structure for CdS is envisioned). We estimate a lower limit of thiolate-capping layer coverage on the CdSe nanoparticles (for which TEM-derived core sizes have been measured), thiolate/NP in Table 2, using the S to Cd ratio according to EDAX in the following equation (eq 1):

$$\text{thiolate/NP} = \frac{p_S \times N_A}{\dfrac{p_{Cd} \times M}{\rho} \times \dfrac{1}{4/3\pi r^3}} \quad (1)$$

Here p_S and p_{Cd} are the atomic percentages of S and Cd according to EDAX, N_A is Avogadro's number, M and ρ are the molecular weight and wurtzite crystal density of CdSe, and r is the TEM-determined CdSe nanoparticle radius (1.5 nm). In comparison, a closely packed thiolate monolayer structure on planar surfaces gives an area per molecule of 21.4 Å².[32] MPA-CdSe is an outlier with the highest apparent surface coverage. This indicates that in this case the thiolate coverage is not monolayer coverage.

Film Structure of n-Carboxylic Acids on HOPG. Representative AFM images of the nanopatterns formed by carboxylic acids with carbon numbers from 14 to 30, $C_{14-30}A$'s,

TABLE 2. List of the Chemical Composition (atom %) and Estimated Thiolate Surface Coverage of the CdSe Nanoparticles Based on EDAX and TEM Results

nanoparticle (synthesis ratio)	Cd (%)	Se or S from NP (%)	S from thiolate (%)	thiolate/NP	area/thiolate (Å²)
MUA-CdSe (3:1)	49.23	38.36	12.41	71.6	39.4
MUA-CdSe (5:1)	48.11	36.07	15.82	94.7	29.8
MPA-CdSe (5:1)	41.58	28.50	29.92	213.6	13.2
MUA-CdS (5:1)	49.23	37.75	13.02	ND	ND
DDT-CdSe (10:1)	41.26	39.41	19.33	123.3	22.9

on HOPG are displayed in Figure 2. We are unable to obtain clear nanopatterns of carboxylic acids shorter than $C_{14}A$ on HOPG by AFM in ambient environment. $C_{14-30}A$'s are capable of self-assembling into the epitaxial nanostripe pattern on HOPG at the monolayer coverage. The 2-D crystalline domains of nanostripes display a rectangular shape whose size, a few hundred nanometers, is determined by the crystalline domain size of HOPG. The orientation of orthogonal stripe domains displays the three-fold symmetry of the HOPG lattice. The stripe thickness, 0.3 ± 0.1 nm, is consistent with the coplanar packing model in which the carbon skeleton plane of the carboxylic acid molecule lies parallel to the HOPG basal plane. All of the nanopatterns formed, ex-
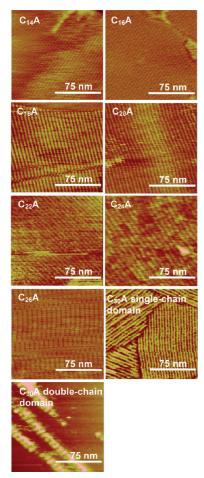
cept that of $C_{30}A$, display a periodicity close to twice the molecular chain length (Table 3), as calculated by the following equation (eq 2):

$$\text{chain length} = \left(\frac{1}{2}\text{number of C atoms per chain} + \frac{1}{2}\text{number of O atoms per carboxyl group}\right) \times 0.246 \text{ nm} \quad (2)$$

The periodicity is consistent with carboxylic acid molecules lying in a head-to-head and tail-to-tail configuration (double-chain domain structure). $C_{30}A$ displays a predominant single-chain domain structure (periodicity = 3.9 nm) with interdispersed double-chain domains (periodicity = 8.0 nm). Such coexisting domains have been observed on $C_{22}A$ on HOPG.[24] A unique film defect in the form of a row or network of holes is observed in the $C_{26}A$ film (Figure 3A−C), which we attribute to packing faults between double-chain and single-chain domains (Figure 3D). The packing fault forms if, instead of aligning the tail to the previous molecular tail in the normal double-chain packing, the molecule points its tail to the opposite direction, which results in antiparallel dimer arrangement in the single-chain domain. The hole-like defect occurs when molecular packing switches between double- and single-chain patterns. It is concluded that the carboxylic acids adopt a persistent epitaxial arrangement on HOPG, which has been reported by others,[23,26,33−35] by spin coating.

Film Structure of *n*-Carboxylic Acids on HOPG in the Presence of Nanoparticles. Nanoparticles are found to induce *n*-carboxylic acid nanorod formation. Using similar film-forming conditions for the generation of MUA-CdSe nanoparticle/$C_{20}A$ nanorod hybrid structure,[28] we show

Figure 2. AFM images of *n*-carboxylic acid monolayers on HOPG. The *z* range is 2 nm for $C_{14-26}A$'s and 10° for $C_{30}A$ single-chain domain and $C_{30}A$ double-chain domain (bright stripes) dispersed in the single-chain domain (smooth area).

TABLE 3. List of Periodicity of the Stripe Pattern by AFM and the Corresponding All-*trans* Molecular Chain Length of Each Carboxylic Acid Studied

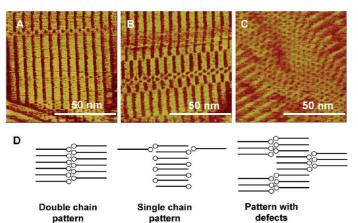| carboxylic acid	periodicity by AFM (nm)	2 × molecular chain length (nm)	domain structure
$C_{14}A$	4.0	3.936	double-chain
$C_{16}A$	4.7	4.428	double-chain
$C_{18}A$	5.0	4.920	double-chain
$C_{20}A$	5.6	5.412	double-chain
$C_{22}A$	6.1	5.904	double-chain
$C_{24}A$	6.6	6.396	double-chain
$C_{26}A$	7.0	6.888	double-chain
$C_{30}A$	8.0/3.9	7.872	double-chain/single-chain

Figure 3. (A−C) AFM phase images of $C_{26}A$ films on HOPG with packing faults. Scan size = 100 nm; z range = 5°. (D) Proposed scheme of the packing fault caused by coexisting double-chain and single-chain packing domains.

that carboxylic acids of different chain length including $C_{14}A$, $C_{16}A$, $C_{18}A$, and $C_{22}A$ can also form nanorods on MUA-CdSe nanoparticles. The results thus demonstrate that the hybrid structure is not limited to the MUA-CdSe/$C_{20}A$ pair in the initial study. In addition, we determine that carboxylic acids with chain length longer than $C_{22}A$ do not readily form nanorods on the nanoparticles. Figure 4 compiles AFM images of n-carboxylic acid films on HOPG in the presence of
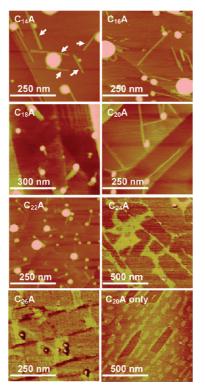

Figure 4. AFM height images of film structure of n-carboxylic acids on HOPG in the presence of MUA-CdSe nanoparticles. Arrows in the $C_{14}A$ image point to doublets or triplets of $C_{14}A$ nanorods. The z range is 8 nm for $C_{14-22}A$'s and 10° for $C_{24}A$ and $C_{26}A$. The bottom-right image is an AFM height image (z range 3 nm) of $C_{20}A$ film with excess partial layers in the absence of the nanoparticles.

TABLE 4. List of the Dimensions of Carboxylic Acid Nanorods As Determined by AFM Sectional Height analysis

carboxylic acid	height of nanorods (Å)	width of nanorods (Å)
$C_{14}A$	9.7 ± 1.2	43.8 ± 3.8
$C_{16}A$	9.7 ± 1.8	50.1 ± 3.4
$C_{18}A$	9.6 ± 0.8	52.6 ± 5.3
$C_{20}A$	9.5 ± 0.9	57.4 ± 3.3
$C_{22}A$	9.4 ± 1.1	62.5 ± 6.4

MUA-CdSe (5:1). Nanoparticle/nanorod objects can generally be found for the shorter n-carboxylic acid chains, but it becomes increasingly difficult to find the hybrid structures for the longer chains. A closer examination of the AFM images shows that the $C_{14}A$ rods contain doublets and triplets of nanorods in a row (marked by the arrows). The doublets and triplets are defined as two and three parallel nanorods in a close-packed structure; that is, the center-to-center separation distance equals the rod diameter. The AFM images show that excess carboxylic acid molecules of $C_{24}A$ and $C_{26}A$ form the 2-D stripe domain instead of nanorods around the nanoparticles. It can be concluded that the presence of the nanoparticles has minimal effect on the ordering of the two longer carboxylic acid molecules. The dimensional analysis results of the nanorods in Table 4 show that the individual nanorods have a fixed height, ~1 nm, a width proportional to the respective chain length, and a stochastic length distribution from 50 to 250 nm. The nanorods only form in the presence of nanoparticles. The bottom-right image in Figure 4 shows a situation when $C_{20}A$ coverage on HOPG is above the monolayer coverage, the excess $C_{20}A$ molecules form epitaxially oriented 2-D stripe domains in the absence of nanoparticles.

The competition between HOPG and the nanoparticle surface in directing the self-assembly of the carboxylic acids can be further modulated by solvents. Fast solvent removal is a prerequisite for the nanorod formation. If the solvent is allowed to slowly evaporate, the film becomes rougher.[36] Nanorods can be observed with a standing time up to 1 min prior to disk spinning. However, the nanorods have a tendency to display orientation along the HOPG lattice, and they tend to form doublets and triplets instead of individual nanorods. With a 5 s standing time of a 2-propanol solution, before spinning, ~75% of the nanorods display a 120° mutual orientation angle. The rate of solvent removal can also be adjusted by the volatility of the solvent. High solvent volatility favors formation of nanorods on the nanoparticle, and the nucleated nanorods are oriented in an increasingly isotropic fashion. For example, using solvents of increasing volatility from ethanol to 1-propanol and to 2-propanol, the percentage of nanorods with three-fold symmetry increases approximately from 13 to 27 and to 65% (Figure 5). It is concluded that fast nucleation and crystallization kinet-
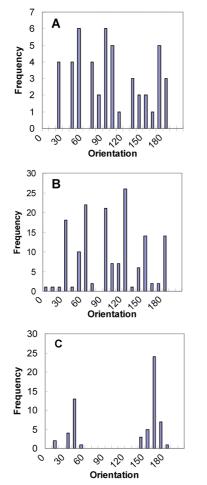
Figure 5. Orientation histogram of $C_{20}A$ nanorods attached to the MUA-CdSe nanoparticle in (A) ethanol, (B) 2-propanol, and (C) 1-propanol. The orientation angle θ of the nanorod is measured by measuring the angle along each nanorod against the horizontal reference line using the angle command in Nanoscope.

ics favor the nanoparticle over the HOPG as a template for the ordering of *n*-carboxylic acids.

In order to determine the salient features of the nanoparticle governing nanorod formation, we investigated different core and shell compositions. We have determined that the chemical nature of the nanoparticle core is immaterial to nanorod formation. Thus, $C_{20}A$ nanorods form on both MUA-CdS and MUA-Au nanoparticles of similar size range and under similar film-forming conditions as MUA-CdSe nanoparticles (Figure 6A,B). On the other hand, when the capping layer, MUA, is replaced with other capping agents, film-forming conditions need to be adjusted accordingly to facilitate nanorod formation. For example, under identical film-forming conditions, MPA-CdSe and DDT-CdSe are ineffective nucleation agents for the nanorods. Both types of nanoparticles have poor colloidal stability in ethanol and propanol. Indeed, MPA-CdSe has a strong tendency to aggregate in all of the solvents studied, and no conditions have been found that would enable nanorods to be induced by MPA-CdSe. The colloidal instability is attributed to the fact that the shorter chain
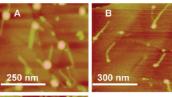

Figure 6. $C_{20}A$ nanorods attached to (A) MUA-CdS, (B) MUA-Au, and (C) DDT-CdSe. The *z* range is 8 nm.

of MPA may be less effective at preventing oxidation and subsequent aggregation.[37] DDT-CdSe nanoparticles, on the other hand, disperse well in nonpolar solvents such as chloroform. Figure 6C shows the nanoparticle/nanorod hybrid structure formed by the DDT-CdSe/$C_{20}A$ pair when chloroform is used as the solvent. We conclude that nanorods form when the thiolate-capping layers permit good dispersion (indicated by the clarity and color intensity of the solution) of the nanoparticles in a chosen solvent. Fully dispersed nanoparticles make the nanoparticle surface available for heterogeneous nucleation. The DDT-CdSe case also refutes a previous hypothesis[28] that specific molecular interactions, for example, the H-bond between the carboxyl group of MUA and that of *n*-carboxylic acids, are responsible for nanorod formation since DDT-CdSe is terminated by methyl group.

We expect the nanoparticle size to be an important factor governing nanorod formation. Generally, we find that the number of nanorods per nanoparticle increases with increasing particle size (as measured by AFM) with a cutoff particle size of ~15 nm. Figure 7 is a plot of the number of individual $C_{20}A$ nanorods per MUA-CdSe (5:1) nanoparticle as a function of d^2 where d is the nanoparticle height as measured by AFM height analysis. It shows a linear relationship between the number of nanorods per particle and the particle surface area (d^2). Nanoparticles larger than 15 nm are ineffective
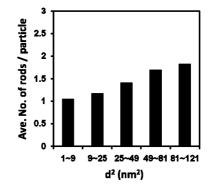

Figure 7. Histogram of the number of multiple nanorods per 2-D crystal as a function of the height of nanoparticle (in 2-propanol). The data contain a standard deviation of 22%.

nucleation seeds. While the majority of the nanorods are single rods for all nanoparticle sizes, there is an increasing occurrence of doublets, triplets, *etc.* (an upper limit of number of closely packed nanorods = 5) with increasing particle size. We also observe the likelihood of multiple nanorod formation to increase with increasing nanoparticle size to carboxylic acid chain length ratio, as the smallest chain, $C_{14}A$, has the highest tendency to form multiple closely packed rods (Figure 4). Approximately 20% $C_{14}A$ nanorods are single rods and the rest are doublets, triplets, *etc.*

DISCUSSION

n-Carboxylic Acid Packing Structure in the Nanorod *versus* Templated on HOPG. Even-numbered long-chain *n*-carboxylic acids possess complex polymorphism, which include the triclinic A- and monoclinic B-, C-, and E-forms.[30,38,39] In all of the forms, the H-bonded dimers of the $R_2^2(8)$ symmetry pack into a bilayer pattern.[40] The main difference between the B- and C-form is that in the B-form the unit cell dimension along the *a*-axis is expanded due to a rotation along the *b*-axis, while in the C-form, the unit cell dimension along the *b*-axis is expanded due to a tilt over the *a*-axis.[41] While both B- and C-forms can be obtained by fast crystallization, kinetics[42] and the solvent ethanol both favor the C-form.[43] We therefore use the C-form crystal structure to interpret the AFM topographical measurement results. The C-form crystal structure of $C_{18}A$ ($P2_1/a$, $Z = 4$) has the following lattice parameters: $a = 0.9360$ nm, $b = 0.4950$ nm, $c = 5.0700$ nm, and $\beta = 128.250°$.[29,41,44] The width of the $C_{18}A$ nanorods by AFM, 5.0 ± 0.6 nm, is consistent with the unit spacing between {001} planes. The height of the nanorods, 1.0 ± 0.1 nm, is slightly larger than the interplanar spacing of the {100} planes (0.74 nm) of the C-form $C_{18}A$ crystal structure. We hypothesize that the rods are formed by carboxylic acid unit cells attaching to each other along the *b* direction during crystallization. Figure 8 shows the crystalline packing structure of the molecular rod in relation to the nanoparticle and the solid surface. The carboxylic acid attaches with its carbon plane parallel to the nanoparticle surface. This is very different from the crystal habit of $C_{18}A$ formed from solution, which displays a thin prismatic plate shape with the most prominent {001} face displaying an acute angle of 54° to the {110} faces. For the molecular nanorods obtained here, the interplanar distances of {001} and {110} are 5.07 and 0.41 nm, respectively. The length direction of the rod is defined by the largest face, the {001} face. The carboxylic acid nanorod possesses the unit cell dimensions (the smallest crystalline unit) in both width and height directions, and it consists of a single bilayer row in the width direction with a H-bonded carboxyl group in the center and terminal methyl groups at the sides. In comparison, in the stripe pattern templated by HOPG, the alkyl chain zigzag plane is parallel to the HOPG basal plane,
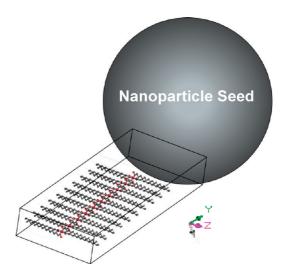

Figure 8. Hypothesized structure of a carboxylic acid molecular rod in the crystalline packing structure of the C-form attached to a nanoparticle nucleation seed.

which presents a smaller layer thickness of 0.3 nm. It is clear that the nanorods are nucleated from the nanoparticle, and they show different packing structure than the stripe pattern templated by HOPG.

Nanorod Formation Mechanism. The spin coating process generates high supersaturation, $\Delta\mu$, which favors the formation of small crystals. In the case of a volatile fluid wetting the HOPG substrate, after an outward flow to produce a smooth film, the last stage of spin coating is dominated by solvent evaporation.[45,46] The film thickness is a function of spin speed, s, initial viscosity, v_0, and evaporation rate, e, as shown in eq 3:[45]

$$h \propto s^{-2/3} v_0^{1/3} e^{1/3} \qquad (3)$$

In our case, the high spin speed combined with low solution concentration results in ultrathin crystalline films reaching the monolayer limit. In addition, fast solvent evaporation results in high $\Delta\mu$, which leads to high nucleation rate, J (defined as the number of nuclei formed per particle per unit time per unit volume), and low crystal growth rate. This "burst" crystallization kinetic model is a common strategy in the synthesis of small and uniform inorganic nanoparticles. According to the classical nucleation theory,[47−49] the critical nucleus size, r_c, decreases with increasing $\Delta\mu$, as shown in eq 4:

$$r_c = \frac{2\Omega\gamma_{CF}}{\Delta\mu} \qquad (4)$$

In the above equation, Ω is the unit volume, and γ_{CF} is the surface free energy of the crystal−fluid interface. Our results suggest that r_c reaches the unit cell dimension (in height and width) of the nuclei at high $\Delta\mu$ (induced by high evaporation rate).

However, we suggest that spin coating alone does not produce the nanorod nanocrystals. In the absence of nanoparticles in solution, 2-D crystallites of

n-carboxylic acids form on HOPG with an epitaxial orientation to the substrate. We surmise that nanoparticles play an essential role in nucleating the nanorod and possibly limiting the growth of the nanorod in the directions normal to the nanorod axis. Particle-mediated nucleation promotes heterogeneous nucleation and plays either a desirable role to control the nucleation process or an undesirable role as impurities. Despite the widespread use of crystallization seeds in material purification, the effect of seed size and composition on nucleation has yet to be understood, particularly when the seed size approaches the critical nucleus size. For example, the minimum seed size requirement for heterogeneous seed-mediated nucleation remains unknown.[50]

According to the classical nucleation theory,[47−49] the presence of a flat foreign surface lowers the nucleation energy barrier from ΔG_0^* to ΔG^* depending on the contact angle, θ, between the cap-shaped nucleus and the planar substrate surface (eq 5):

$$\frac{\Delta G^*}{\Delta G_0^*} = f = \frac{1}{4}(1 - \cos\theta)^2(2 + \cos\theta) \qquad (5)$$

Here, $\cos\theta = (\gamma_{SF} - \gamma_{SC})/\gamma_{CF}$, where γ_{SF}, γ_{SC}, and γ_{CF} are the substrate/fluid, substrate/crystal, and crystal/fluid interfacial tension, respectively. The nucleation capability of a substrate surface, which is defined by f, diminishes (f approaches the upper limit value of 1) if the substrate is a particle with a small radius of curvature, R^S; f is a function of θ and the normalized particle radius of curvature $R' = R^S/r_c$,[51−53] in which R^S is the radius of curvature of the seed particle. When the particle is large (e.g., $R' \geq 10$), the particle surface curvature approaches that of a flat surface, and the energy barrier is dominated by θ. When the particle is small (e.g., $R' \leq 0.1$), f is close to 1, and the foreign particle is ineffective in nucleation. When $0.1 \leq R' \leq 10$, f decreases drastically with decreasing r_c (or increasing $\Delta\mu$). Therefore, small r_c or the presence of a good structural match compensates for the small seed size so that even nanoparticles can be effective nucleation substrates. In addition, small seed particles with high curvature dominate nucleation kinetics at high $\Delta\mu$.

Considering only the interfacial energy term, θ goes to zero when γ_{SF} is close to γ_{CF}. This will be the case when the chemical nature of the crystal is similar to that of the substrate. In heterogeneous nucleation, the presence of a foreign particle surface that is completely wetted by the nucleating fluid will reduce the nucleation energy barrier to zero. A good dispersion of the nanoparticle seeds in the crystallizing fluid allows a complete wetting of the seed surface by the fluid. This is governed by the chemical characteristics of the surface, which can be modulated by introducing capping ligands of suitable polarity.

Next we consider the elastic energy term. Our results show a possible competition between nanoparti-

cle and HOPG substrates for the carboxylic acid crystal nucleation. At low $\Delta\mu$, J is dominated by the epitaxial match between the carbon chain plane and the basal plane of HOPG, which lowers the nucleation energy. In the competition between HOPG- and nanoparticle-mediated molecular ordering, longer carbon chain length on the part of the n-carboxylic acid favors the epitaxial interaction with HOPG because the epitaxial interaction with HOPG increases with increasing chain length. Thus, the epitaxial mismatch between the HOPG lattice and carboxylic acid molecules in the randomly oriented nanorods nucleated from the nanoparticle becomes increasingly prohibitive for nanorods composed of longer chains.

The nanoparticle-induced nanorod formation is also consistent with the molecular simulation results of colloidal crystallization that identify a critical seed size.[50,54] The simulations show that seed-mediated nucleation occurs only when the seed particle (substrate) radius is at least 5 times the size of the colloidal particles (crystallizing species). Interestingly, snapshots of the nuclei of increasing size show that the initial colloidal cluster tends to wrap around the seed as a 2-D layer when the seed size is 7 times that of the colloid. However, the cluster becomes a radially oriented "1-D" rod when the seed size is 5 times that of the colloid. The authors hypothesize that the radially elongated cluster is induced by the high curvature of the small seed, which imposes an unsustainable strain for tangential growth. The length scale of our system may not be pertinent to the colloidal crystallization simulated, but our observation of the 1-D rods is consistent with the 1-D clusters in the simulations.

In comparison to the energetic considerations, nucleation kinetics may be more important for the nanorod formation. The nanorod structure with a poorer structural match than the 2-D stripe domains may represent a kinetically more favored state at high $\Delta\mu$. At high $\Delta\mu$, J is dominated by the pre-exponential collision/attachment factor, K, and less by the exponential energy barrier term in the following expression (eq 6):

$$J = K\exp(-\Delta G^*/kT) \qquad (6)$$

In particle-mediated nucleation, J is proportional to the number and size of the nanoparticle seeds because nucleation occurs in the solution layer adjacent to the particle surface. We find that the nucleation rate per particle, J_P, as represented by the number of nanorods per particle on an AFM image, is indeed proportional to the nanoparticle surface area, $(R_i^S)^2$ or d^2 in Figure 7, where d is the nanoparticle height as measured by AFM height analysis.

A closer examination of the AFM images shows roughly two populations of nanorods. A majority of the nanorods are oriented along the radial direction of the particle while the rest adopt a tangential orienta-

tion. Their relative percentage, RP, is close to 1 (eq 7):

$$RP = \frac{\text{number of tangential nanorods}}{\text{number of radial nanorods}} = \frac{84}{77} = 1.09$$

(7)

The similar distribution of the two orientations is consistent with equal attachment probability of carboxyl dimers in the tangential and radial orientations to the particle seed surface. The similar size of the tangentially oriented nanorods and the radially oriented nanorods suggests that at least in this case the strain energy caused by misalignment of carboxylic acid nanorods on carboxylic acid monolayer-covered HOPG plays the more dominant role in limiting crystal growth width direction than the curvature constraint placed by the nanoparticle.

CONCLUSIONS

The work demonstrates a methodology of using monolayer-protected inorganic nanoparticles as nucleation seeds for the creation of extremely narrow organic nanorods. The hybrid nanoparticle/nanorod architecture deposited on HOPG is characterized by AFM. The carboxylic acid nanorods are 50−250 nm in length with cross sections of dimensions similar to the a- and c-axes of the C-form crystals. It is deduced from the cross-sectional topographical analysis that a single H-bonded carboxyl dimer spans the width of the nanorod and they pack in a coplanar crystalline structure along the long axis of the nanorod. Nanoparticles of different core materials (CdSe, CdS, and Au) but with the same capping ligand (MUA) are capable of inducing identical carboxylic acid nanorods. We further determine that nanoparticles with methyl terminal groups are also capable of inducing the nanorod structure if a compatible solvent is used. Variation of the carboxylic acid chain length reveals a competitive crystallization templating process between the nanoparticle surface and the HOPG basal plane. The narrow width of the nanorod is attributed to two energetic factors. There is a significant mismatch between the carbon chain plane and HOPG for randomly oriented nuclei, which prevents the attachment of carboxyl dimers along the carbon chain direction (the c-axis). The second factor is the high strain energy as a result of the highly curved surface of the nanoparticle in the tangential direction of the seed surface. A rough estimate of nucleation rate per nanoparticle shows that the kinetics of nanoparticle-mediated nanorod formation is consistent with the prediction from the classical nucleation theory. The nucleation rate is proportional to the surface area of the seed substrate. This work shows that, contrary to the common belief that particles of nanometer size have diminished effect in heterogeneous nucleation, they indeed are capable of nucleating and constraining the shape of molecular crystals. Imaging and probing the impact of size and shape of the critical clusters provides new insights into heterogeneous seed-mediated crystallization where few details are known. Moreover, it enables us to create and control the formation of unique hybrid nanostructures that employ the dual functionalities of the inorganic nanoparticle and organic nanorod.

METHODS

Materials. *Film Formation.* Dodecanoic acid ($C_{12}A$, Aldrich, 98%), tetradecanoic acid ($C_{14}A$, Sigma, 99−100%), hexadecanoic acid ($C_{16}A$, Aldrich, 99%), octadecanoic acid ($C_{18}A$, Fluka, ≥ 99.5%), eicosanoic acid ($C_{20}A$, Sigma, ≥ 99%), docosanoic acid ($C_{22}A$, Aldrich, 99%), tetracosanoic acid ($C_{24}A$, Fluka, ≥ 99.0%), hexacosanoic acid ($C_{26}A$, Sigma, ≥ 95%), and triacontanoic acid ($C_{30}A$, Sigma, ≥ 95%) are used. Solvents used include methanol (Mallinckrodt Chemicals, 100%), ethanol (Pharmco, 100%), 1-propanol (Fisher Scientific, 100%), 2-propanol (Mallinckrodt Chemicals, 100%), and chloroform (Fisher Scientific, 100%). HOPG (Mikromasch, ZYB grade) is hand-cleaved just before use with an adhesive tape until a smooth surface is obtained.

Nanoparticle Synthesis. Trioctylphosphine oxide (TOPO, 90%), selenium powder (99.5%), 11-mercaptoundecanoic acid (MUA, 95%), and tetranitromethane are purchased from Aldrich. Tetramethylammonium hydroxide pentahydrate (TMAH, 99%) is purchased from Acros organics. Cadmium oxide (CdO, 99.9%) and trioctylphosphine (TOP, 97%) are obtained from Strem Chemicals. 1-Tetradecylphosphonic acid (98%) is obtained from Alfa-Aesar. Additional solvents used are toluene and ethyl acetate, purchased from Fisher.

Nanoparticle Synthesis and Surface Modification. The synthesis of CdSe and CdS nanoparticles is adapted from Peng *et al.*[55] The thiolate-capping procedure follows a modified procedure by Aldana *et al.*[56] The thiol-capped gold nanoparticles are synthesized using a sodium borohydride aqueous solution for the reduction of tetrachloroauric acid followed by reaction with the thiol.[57] The following nanoparticles are studied: CdSe capped by 3-mercaptopropionic acid (MPA-CdSe), CdSe capped by 11-mercaptoundecanoic acid (MUA-CdSe), CdSe capped by 1-dodecanethiol (DDT-CdSe), CdS capped by MUA (MUA-CdS), and Au capped by MUA (MUA-Au).

Film Preparation. A freshly made solution of the carboxylic acid (0.1 mL) with a concentration range of 0.05−0.4 mM (adjusted by trial and error depending on solubility of the particular carboxylic acid) is used in each spin coating experiment in order to deposit close to a monolayer quantity on HOPG. The spin rate is 3000 rpm, and the spin time is 60 s. To study the effect of the nanoparticle, mixed solutions containing both the carboxylic acid and the nanoparticle are used. The nanoparticle concentration in the mixed solution is maintained at 0.1 mM (based on Cd), while the carboxylic acid concentration is maintained at 0.05−0.4 mM. The nanostructure of the films is unchanged when kept in the laboratory environment for at least 1 month.

Characterization. The following instruments are used: AFM (Dimension 3100, Veeco), transmission electron microscopy (TEM, JEOL 2010F TEM), and *in situ* energy-dispersive spectroscopy (EDS, EDAX) attached to a Hitachi S-2400 SEM.

The nanoparticle size is determined by TEM and AFM. TEM is conducted in the bright-field mode operating at an accelerating voltage of 200 keV. Particle sizes are averaged over 80−100 individual nanoparticles by manually measuring each particle diameter from the TEM images. The particle size averages are also obtained using the AFM sectional height analysis command (Nanoscope) by manually measuring the lateral diameters and vertical heights of 80−100 particles on HOPG (or mica). The lateral diameter of a particle is determined at the full width

at half-maximum height in order to minimize tip convolution.[58] Unlike TEM, AFM-measured particle sizes include the thiolate-capping layer.

The elemental composition of the nanoparticles with the capping layer is obtained by EDS analysis. The nanoparticles are sprinkled on carbon adhesive tabs placed on an aluminum stub, and EDS data are acquired at 25 keV in the secondary electron mode of the SEM.

The spin-coated thin film nanostructure is imaged by a Dimension 3100 AFM in the tapping mode in ambient air. The height, amplitude, and phase images are obtained using silicon tapping tips (nanoScience Instruments, VistaProbes T300) with a resonance frequency of 300 kHz and a tip radius less than 10 nm. Height images are plane-fit in the fast scan direction with no additional filtering operation. The periodic pattern of the carboxylic acid films is analyzed by the 2-D fast Fourier transform (2D FFT) command, while the nanoparticle and nanorod dimensions are analyzed by the sectional height analysis command.

REFERENCES AND NOTES

1. Clarke, S. M. Neutron Diffraction and Incoherent Neutron Scattering from Adsorbed Layers. *Curr. Opin. Colloid Interface Sci.* **2001**, *6*, 118–125.
2. De Feyter, S.; De Schryver, F. C. Self-Assembly at the Liquid/Solid Interface: STM Reveals. *J. Phys. Chem. B* **2005**, *109*, 4290–4302.
3. Orlin, D. V.; Shalini, G. Materials Fabricated by Micro- and Nanoparticle Assembly—The Challenging Path from Science to Engineering. *Adv. Mater.* **2009**, *21*, 1897–1905.
4. Sachin, K.; Mercedes, C.-C.; David, N. R. Self-Assembling Nanoparticles at Surfaces and Interfaces. *ChemPhysChem* **2008**, *9*, 20–42.
5. Shipway, A. N.; Katz, E.; Willner, I. Nanoparticle Arrays on Surfaces for Electronic, Optical, and Sensor Applications. *ChemPhysChem* **2000**, *1*, 18–52.
6. Fendler, J. H. Chemical Self-Assembly for Electronic Applications. *Chem. Mater.* **2001**, *13*, 3196–3210.
7. Kickelbick, G. Concepts for the Incorporation of Inorganic Building Blocks into Organic Polymers on a Nanoscale. *Prog. Polym. Sci.* **2003**, *28*, 83–114.
8. Adams, D. M.; Brus, L.; Chidsey, C. E. D.; Creager, S.; Creutz, C.; Kagan, C. R.; Kamat, P. V.; Lieberman, M.; Lindsay, S.; Marcus, R. A.; *et al.* Charge Transfer on the Nanoscale: Current Status. *J. Phys. Chem. B* **2003**, *107*, 6668–6697.
9. Saavedra, H. M.; Mullen, T. J.; Zhang, P. P.; Dewey, D. C.; Claridge, S. A.; Weiss, P. S. Hybrid Strategies in Nanolithography. *Rep. Prog. Phys.* **2010**, *73*, 036501.
10. Andrew, R. H.; Beatriu, E.; Juan, F. M.; David, K. S. High-Tech Applications of Self-Assembling Supramolecular Nanostructured Gel-Phase Materials: From Regenerative Medicine to Electronic Devices. *Angew. Chem., Int. Ed.* **2008**, *47*, 8002–8018.
11. Eugenii, K.; Itamar, W. Integrated Nanoparticle−Biomolecule Hybrid Systems: Synthesis, Properties, and Applications. *Angew. Chem., Int. Ed.* **2004**, *43*, 6042–6108.
12. Ana, B. D.; Ramón, M.-M.; Félix, S.; Katrin, H.; Knut, R. The Supramolecular Chemistry of Organic−Inorganic Hybrid Materials. *Angew. Chem., Int. Ed.* **2006**, *45*, 5924–5948.
13. Nikoobakht, B.; Wang, Z. L.; El-Sayed, M. A. Self-Assembly of Gold Nanorods. *J. Phys. Chem. B* **2000**, *104*, 8635–8640.
14. Yang, P. D.; Kim, F. Langmuir−Blodgett Assembly of One-Dimensional Nanostructures. *ChemPhysChem* **2002**, *3*, 503–506.
15. Dieter Horn, J. R. Organic Nanoparticles in the Aqueous Phase—Theory, Experiment, and Use. *Angew. Chem., Int. Ed.* **2001**, *40*, 4330–4361.
16. Nguyen, T. Q.; Martel, R.; Avouris, P.; Bushey, M. L.; Brus, L.; Nuckolls, C. Molecular Interactions in One-Dimensional Organic Nanostructures. *J. Am. Chem. Soc.* **2004**, *126*, 5234–5242.
17. Brousseau, L. C.; Zhao, Q.; Shultz, D. A.; Feldheim, D. L. pH-Gated Single-Electron Tunneling in Chemically Modified Gold Nanoclusters. *J. Am. Chem. Soc.* **1998**, *120*, 7645–7646.
18. Chondroudis, K.; Mitzi, D. B. Electroluminescence from an Organic−Inorganic Perovskite Incorporating a Quaterthiophene Dye within Lead Halide Perovskite Layers. *Chem. Mater.* **1999**, *11*, 3028–3030.
19. Mirkin, C. A.; Letsinger, R. L.; Mucic, R. C.; Storhoff, J. J. A DNA-Based Method for Rationally Assembling Nanoparticles into Macroscopic Materials. *Nature* **1996**, *382*, 607–609.
20. Besteman, K.; Lee, J. O.; Wiertz, F. G. M.; Heering, H. A.; Dekker, C. Enzyme-Coated Carbon Nanotubes as Single-Molecule Biosensors. *Nano Lett.* **2003**, *3*, 727–730.
21. Shi, Y.; Yang, R. Z.; Yuet, P. K. Easy Decoration of Carbon Nanotubes with Well Dispersed Gold Nanoparticles and the Use of the Material as an Electrocatalyst. *Carbon* **2009**, *47*, 1146–1151.
22. Yildiz, H. B.; Tel-Vered, R.; Willner, I. Solar Cells with Enhanced Photocurrent Efficiencies Using Oligoaniline-Crosslinked Au/CdS Nanoparticles Arrays on Electrodes. *Adv. Funct. Mater.* **2008**, *18*, 3497–3505.
23. Rabe, J. P.; Buchholz, S. Commensurability and Mobility in 2-Dimensional Molecular-Patterns on Graphite. *Science* **1991**, *253*, 424–427.
24. Kuroda, R.; Kishi, E.; Yamano, A.; Hatanaka, K.; Matsuda, H.; Eguchi, K.; Nagagiri, T. Scanning Tunneling Microscope Images of Fatty Acid Langmuir−Blodgett Bilayers. *J. Vac. Sci. Technol., B* **1991**, *9*, 1180–1183.
25. Kishi, E.; Matsuda, H.; Kuroda, R.; Takimoto, K.; Yamano, A.; Eguchi, K.; Hatanaka, K.; Nakagiri, T. Barrier-Height Imaging of Fatty-Acid Langmuir−Blodgett-Films. *Ultramicroscopy* **1992**, *42*, 1067–1072.
26. Hibino, M.; Sumi, A.; Tsuchiya, H.; Hatta, I. Microscopic Origin of the Odd−Even Effect in Monolayer of Fatty Acids Formed on a Graphite Surface by Scanning Tunneling Microscopy. *J. Phys. Chem. B* **1998**, *102*, 4544–4547.
27. Mao, G.; Dong, W.; Kurth, D. G.; Mohwald, H. Synthesis of Copper Sulfide Nanorod Arrays on Molecular Templates. *Nano Lett.* **2004**, *4*, 249–252.
28. Chen, D.; Wang, R.; Arachchige, I.; Mao, G.; Brock, S. L. Particle-Rod Hybrids: Growth of Arachidic Acid Molecular Rods from Capped Cadmium Selenide Nanoparticles. *J. Am. Chem. Soc.* **2004**, *126*, 16290–16291.
29. Kaneko, F. Polymorphism and Phase Transitions of Fatty Acids and Acylglycerols. In *Crystallization processes in fats and lipid systems*; Garti, N., Sato, K., Eds.; Marcel Dekker: New York, 2001; pp 53−97.
30. Bond, A. D. On the Crystal Structures and Melting Point Alternation of the *n*-Alkyl Carboxylic Acids. *New J. Chem.* **2004**, *28*, 104–114.
31. Wan, L.; Manickam, D. S.; Oupicky, D.; Mao, G. Z. DNA Release Dynamics from Reducible Polyplexes by Atomic Force Microscopy. *Langmuir* **2008**, *24*, 12474–12482.
32. Ulman, A. Formation and Structure of Self-Assembled Monolayers. *Chem. Rev.* **1996**, *96*, 1533–1554.
33. Wu, Y.; Cheng, G.; Katsov, K.; Sides, S. W.; Wang, J.; Tang, J.; Fredrickson, G. H.; Moskovits, M.; Stucky, G. D. Composite Mesostructures by Nano-Confinement. *Nat. Mater.* **2004**, *3*, 816–822.
34. Tao, J.; Mao, G. Z.; Daehne, L. Asymmetrical Molecular Aggregation in Spherulitic Dye Films. *J. Am. Chem. Soc.* **1999**, *121*, 3475–3485.
35. Yang, T.; Berber, S.; Liu, J. F.; Miller, G. P.; Tomanek, D. Self-Assembly of Long Chain Alkanes and Their Derivatives on Graphite. *J. Chem. Phys.* **2008**, *128*, 124709.
36. Byung Gil, J.; Seok-Hong, M.; Chang-Woo, K.; Sang-Hyun, P.; Ki-Bum, K.; Tae-Sik, Y. Colloidal Nanoparticle-Layer Formation Through Dip-Coating: Effect of Solvents and Substrate Withdrawing Speed. *J. Electrochem. Soc.* **2009**, *156*, K86–K90.

37. Arachchige, I. U.; Brock, S. L. Sol−Gel Methods for the Assembly of Metal Chalcogenide Quantum Dots. *Acc. Chem. Res.* **2007**, *40*, 801–809.

38. Moreno, E.; Cordobilla, R.; Calvet, T.; Cuevas-Diarte, M. A.; Gbabode, G.; Negrier, P.; Mondieig, D.; Oonk, H. A. J. Polymorphism of Even Saturated Carboxylic Acids from *n*-Decanoic to *n*-Eicosanoic Acid. *New J. Chem.* **2007**, *31*, 947–957.

39. Kaneko, F.; Kobayashi, M.; Kitagawa, Y.; Matsuura, Y. Collective Displacement of Acyl Chains on E→C Phase-Transition of Stearic-Acid. *J. Phys. Chem.* **1992**, *96*, 7104–7107.

40. Bernstein, J.; Davis, R. E.; Shimoni, L.; Chang, N. L. Patterns in Hydrogen Bonding—Functionality and Graph Set Analysis in Crystals. *Angew. Chem., Int. Ed. Engl.* **1995**, *34*, 1555–1573.

41. Malta, V.; Celotti, G.; Zannetti, R.; Martelli, A. F. Crystal Structure of the C Form of Stearic Acid. *J. Chem. Soc. B* **1971**, *75*, 548–553.

42. Meine, K.; Weidemann, G.; Vollhardt, D.; Brezesinski, G.; Kondrashkina, E. A. Atomic Force Microscopy and X-ray Studies of Three-Dimensional Islands on Monolayers. *Langmuir* **1997**, *13*, 6577–6581.

43. Sato, K.; Okada, M. Growth of Large Single Crystals of Stearic Acid from Solution. *J. Cryst. Growth* **1977**, *42*, 259–263.

44. CCDC STARAC01 contains the supplementary crystallographic data of stearic acid C-form. It can be obtained free of charge *via* www.ccdc.cam.ac.uk/data_request/cif, or by emailing support@ccdc.cam.ac.uk.

45. Meyerhofer, D. Characteristics of Resist Films Produced by Spinning. *J. Appl. Phys.* **1978**, *49*, 3993–3997.

46. Bornside, D. E.; Macosko, C. W.; Scriven, L. E. Spin Coating—One-Dimensional Model. *J. Appl. Phys.* **1989**, *66*, 5185–5193.

47. Becker, R.; Döring, W. Kinetische Behandlung der Keimbildung in übersättigten Dämpfen. *Ann. Phys.* **1935**, *24*, 719–752.

48. Volmer, M. *Kinetik der Phasenbildung*; Steinkopff: Leipzig, 1939.

49. Kashchiev, D. *Nucleation*; Butterworth-Heinemann: Oxford, 2000.

50. Cacciuto, A.; Auer, S.; Frenkel, D. Onset of Heterogeneous Crystal Nucleation in Colloidal Suspensions. *Nature* **2004**, *428*, 404–406.

51. Fletcher, N. H. Size Effect in Heterogeneous Nucleation. *J. Chem. Phys.* **1958**, *29*, 572–576.

52. Liu, X. Y. *Generic Mechanism of Heterogeneous Nucleation and Molecular Interfacial Effects*; Elsevier Sci. B.V.: Amsterdam, 2001.

53. Liu, X. Y. Generic Progressive Heterogeneous Processes in Nucleation. *Langmuir* **2000**, *16*, 7337–7345.

54. Cacciuto, A.; Frenkel, D. Simulation of Colloidal Crystallization on Finite Structured Templates. *Phys. Rev. E* **2005**, *72*, 041604.

55. Peng, Z. A.; Peng, X. Formation of High-Quality CdTe, CdSe, and CdS Nanocrystals Using CdO as Precursor. *J. Am. Chem. Soc.* **2000**, *123*, 183–184.

56. Aldana, J.; Wang, Y. A.; Peng, X. G. Photochemical Instability of CdSe Nanocrystals Coated by Hydrophilic Thiols. *J. Am. Chem. Soc.* **2001**, *123*, 8844–8850.

57. Chirea, M.; Pereira, C. M.; Silva, F. Catalytic Effect of Gold Nanoparticles Self-Assembled in Multilayered Polyelectrolyte Films. *J. Phys. Chem. C* **2007**, *111*, 9255–9266.

58. Fritzsche, W.; Schaper, A.; Jovin, T. M. Probing Chromatin with the Scanning Force Microscope. *Chromosoma* **1994**, *103*, 231–236.